Numerical Simulation of Nitrogen Oxide Formation in Lean Premixed Turbulent $H_2/O_2/N_2$ Flames

Marc S. Day[a], John B. Bell[a], Xinfeng Gao[a], and Peter Glarborg[b]

[a]Lawrence Berkeley National Laboratory, Berkeley, CA 94720, USA
[b]Department of Chemical Engineering, Technical University of Denmark, DK-2800, Lyngby, Denmark

---

Abstract

Lean premixed hydrogen flames are thermodiffusively unstable and burn in cellular structures. Within these cellular structures the flame is locally enriched by preferential diffusion of H_2. This local enrichment leads to hot spots in which the flame burns with considerably more intensity than the corresponding laminar flame. In this paper we investigate the impact of this local enrichment on the formation of emissions of oxides of nitrogen. We consider a two dimensional configuration in which premixed H_2-air flames interact with a weakly turbulent velocity field for a range of equivalence ratios. The simulations show that although the peak temperatures in the hot spots remain well below 1800K where thermo NO_x becomes significant, the hot spots are the location of the dominant production of emissions. Furthermore, the turbulent flames all show increased emissions compared to the flat laminar flames. with the relative increase in emissions becoming more significant at lower equivalence ratios. A more detailed examination of the reaction chemistry shows that at richer conditions the predominant path for the initiation of emissions is $N_2 \rightarrow NNH$. As the flame becomes leaner $N_2 \rightarrow N_2O$ becomes increasing important.

Keywords: premixed lean combustion, turblent combustion, nitrogen oxide formation

---

1. Introduction

There has been considerable recent interest in the development of fuel-flexible premixed turbine combustors that are capable of burning lean hydrogen or hydrogen-enriched lean hydrocarbon fuels (e.g., [1–4]). Devices based on lean premixed fuels generate substantially lower NO_x emissions than equivalent nonpremixed or stoichiometric premixed systems [5]. For these fuels, NO_x is produced primarily through the thermal mechanism [5, 6], and the reduction in emissions is believed to be a direct consequence of the lower post-flame gas temperatures.

Recent laboratory experiments have shown that ultra-lean hydrocarbon flames (with fuel concentrations well below lean blow-off limits) can in fact be stabilized in a turbulent burner if the fuel mixture is enriched with H_2 [2]. Hydrogen addition enhances the effective flame speed and auto-ignition processes of the mixture, [7], both of which lead to an increased resistence to strain-induced extinction. However, NO_x emission levels do not decrease uniformly with increasing hydrogen enrichment, relative to the hydrocarbon fuel. In a recent experimental study [1], pure H_2-air flames exhibited a pronounced "floor" at 1 ppm NO in the exhaust stream, below which further reduction in the adiabatic post-flame gas temperature had no effect on the measured emissions. Moreover, this "floor" was a factor of two or three higher than values produced in the same burner using ultra-lean hydrocarbon mixtures (seeded with hydrogen) that had comparable post-flame gas temperatures. The experimental data for pure H_2 mixtures was taken at 8 atm, and the post-flame temperature was controlled by adjusting the air content of the premixed fuels. The range of fuels were burned in a low-swirler injector configuration and the tests were designed to evaluate the low-swirl nozzle for fuel-flexible applications at turbine conditions.

We conjecture that the observed floor in NO_x emissions is directly linked to the thermodiffusively unstable nature of premixed hydrogen combustion. The thermodiffusive instability leads to cellular burning structures as noted in early work by Markstein [8] and Zeldovich [9]. Cellular burning patterns have been observed experimentally in lean H_2/O_2 mixtures by many researchers (see, for example, Bregeon et al. [10] and Mitani and Williams [11]). These relatively robust flame features are characterized by intensely-burning hotspots that coincide with localized enhancement of the fuel-to-oxidizer ratio that is driven by differences in diffusivities (see [12] and the references cited therein). These hotspots often burn at temperatures considerably in excess of the adiabatic flame temperature of the mean mixture, separated by narrow zones of persistent flame extinction. In this highly nonuniform environment, the net global production of NO_x then becomes a sum of local enhancement near super-heated gas and local suppression near extinguished pockets. The tendency to form these structures, and their size and separation as they propagate through the fuel mixture, is a function of the hydrogen-to-oxygen ratio. The resulting impact on NO_x production across a range of enrichments in a combustor is not easily estimated.

The goal of this paper is to quantify the emission formation and identify the governing mechanisms in lean premixed hydrogen-air flames. We consider a two-dimensional configuration in which we examine the interaction of lean premixed hydrogen flames with weak two-dimensional turbulence. The simulations use a feedback control mechanism [13] to stabilize the flow and generate a quasi-steady, but time-dependent evolution of the cellular flame structures that form naturally in these low-*Le* mixtures. In the next section, we review our computational approach and describe the study in more detail. We then provide an overview of the flames that result and characterize their NO_x-generation behavior. Finally, we examine the nitrogen chemistry in a neighborhood of the cellular flame hotspots.

2. Computational Framework

The simulations reported here are performed with the adaptive low Mach number algorithm presented in Day and Bell [14]. The model treats the fluid as a mixture of perfect gases with a mixture model for diffusion, and ignores Soret, Dufour, gravitational and radiative transport effects. A detailed chemical description containing 15 species and 58 reversible Arrhenius reactions is used to describe premixed hydrogen-air combustion and subsequent NO_x formation. This mechanism was derived by rate-of-production and sensitivity analyses from a full reaction mechanism [15, 16] to obtain the minimum reaction set that describes NO formation in H_2 oxidation at lean conditions ($\phi \approx 0.37$) in the temperature range 1100-1600 K. It involves NO formation through NNH and N_2O, as well as thermal NO. The nitrogen-related reactions in the model is listed in Table 1.

With these assumptions, the system of low Mach number flow equations for an open domain is

$$\frac{\partial \rho U}{\partial t} + \nabla \cdot \rho U U = -\nabla \pi + \nabla \cdot \tau,$$

$$\frac{\partial \rho Y_m}{\partial t} + \nabla \cdot U \rho Y_m = \nabla \cdot \rho D_m \nabla Y_m + W_m \dot{\omega}_m,$$

$$\frac{\partial \rho h}{\partial t} + \nabla \cdot U \rho h = \nabla \cdot \frac{\lambda}{c_p} \nabla h$$

$$+ \sum_m \nabla \cdot h_m \Big(\rho D_m - \frac{\lambda}{c_p} \Big) \nabla Y_m,$$

where ρ is the gas mixture density, U is the gas mixture velocity, Y_m is the mass fraction of species m, h is the mass-weighted enthalpy of the gas mixture, T is the mixture temperature, and $\dot{\omega}_m$ is the net molar production rate for species m due to chemical reactions:

$$\dot{\omega}_m = \sum_j \dot{\omega}_{m,j} = \sum_j \nu_{m,j} q_j$$

where $\nu_{m,j}$ is the moles of m created per reaction j, and q_j is the progress rate of reaction j. Also, W_m is the molecular mass of species m, λ is the thermal conductivity, τ is the stress tensor, c_p is the specific heat of the mixture, and $h_m(T)$ and D_m are the enthalpy and mixture-averaged diffusion coefficients of species m, respectively. In the low Mach number model π is the perturbational pressure field ($\pi/p_0 \sim \mathcal{O}(M^2)$), where M is the Mach number. These evolution equations are supplemented by an equation of state for a perfect gas mixture:

$$p_0 = \rho R_{mix} T = \rho \mathcal{R} T \sum_m \frac{Y_m}{W_m}$$

where $\mathcal{R}$ is the universal gas constant. In the low Mach number model, there is no acoustic wave transport, and the equations of state serves to constrain the evolution of the flow.

The basic discretization combines a symmetric operator-split treatment of chemistry and transport with a density-weighted approximate projection method. The projection method is used to impose a constraint on the velocity divergence such that a conservative integration of the species mass and total enthalpy simultaneously satisfies the equation of state. Time integration of the algorithm proceeds on the scale of the relatively slow advective transport. Faster diffusion and chemistry processes are treated time-implicitly. This integration scheme is embedded in a parallel adaptive mesh refinement algorithm framework based on a hierarchical system of rectangular grid patches. The overall integration algorithm is second-order accurate in both space and time, and discretely conserves species mass and enthalpy.

The flow configuration we consider initializes a laminar flame in a rectangular domain, 8cm × 16cm, oriented so that the flame propagates downward. A cold fuel-air mixture enters the domain through bottom boundary, and hot combustion products exit the domain through the top. The remaining computational boundaries are periodic. Along the inflow face we use a feedback control algorithm [13] to dynamically adjust the mean gas inflow velocity so that the mean flame location remains stationary within the domain over time. For the calculations presented here, we set the mean flame location 3 cm above the inflow face. Turbulent fluctuations are introduced into the inlet flow by superimposing a pre-computed zero-mean fluctuating velocity field onto the time-dependent boundary value. In an auxiliary calculation the fluctuations for this purpose were initialized using a random velocity field with a prescribed energy spectrum [17]

$$E(k) = \frac{(\frac{k}{k_i})^4}{[1 + (\frac{k}{k_i})^2]^{\frac{17}{6}}} e^{-\frac{9}{4}(\frac{k}{k_d})^{\frac{4}{3}}}$$

where k is the wavenumber, k_d = 6400 cm^{-1} and k_i = 65 cm^{-1}. The random field was then evolved using an incompressible flow solver to adjust the phasing of the velocity fields. The resulting synthetic turbulence is isotropic with an integral scale $\ell_t = 3.0$ mm and a turbulent intensity, $u' = 18.5$ cm/s. The reacting flow simulations are run until the flame is statistically stationary prior to analysis. We consider three different equivalence ratios, $\phi =$ 0.30, 0.37 and 0.45. The mean inlet velocity in each case varies over time in response to the development of the wrinkled flame surface, but is roughly 40, 55 and 90 cm/s, for $\phi =$ 0.30, 0.37 and 0.45 respectively.

The simulations are carried out with a 4-level dynamically adaptive grid hierarchy, where each successive level consists of cells a factor of two smaller in each direction. The coarsest level, covering the entire domain, consists of 256×512 uniform cells. The finest level, with $\Delta x = 39\mu$m, tracks the flame surface (regions of high H_2 consumption rate). Regions of high vorticity are refined to $\Delta x = 78\mu$m. Each level remains nested in the next coarser level, and the numerical timestep at each level satisfies a level-appropriate CFL-type constraint. This level of refinement, in space and time, is more than adequate to ensure numerical convergence of the results presented next.

3. Results and Discussions

Typical snapshots of quasi-steady flames from each of the three cases are shown in Figure 1. For each case we show the temperature field, and the mole fractions of OH, NO and N_2O. White boxes drawn on these plots indicate 9 mm × 9 mm subregions extracted from each case for discussions later in this section. The species OH is a flame radical, and its concentration is correlated to local fuel consumption rates in these lean flames [18]. The OH profiles clearly illustrate the cellular structure of the flames, with more intense burning in regions of positive curvature (center of curvature in the products). The temperature plots show localized hotspots in regions corresponding to the cellular burning structures.

The gross pattern of burning structures (i.e., the “flame shape”) results from the interaction of the turbulent fluctations with the thermodiffusive and hydrodynamic instabilities. The flames show the cellular patterns of intense burning separated by gaps where the flame is locally extinguished that are characteristic of the low Lewis number of the fuel, overlaid with larger-scale wrinkling characteristic of interaction with vortical structures and the hydrodynamic instability [19]. With increasing equivalence ratio, the flames generally exhibit smaller spatial scales; the burning regions are narrower, both transverse and parallel to the local temperature gradient, and are separated by narrower gaps.

In the post-flame region of all three cases, the bulk of the nitrogen-oxides takes the form of NO and N_2O. The level of NO is of the order of 1 ppm, similar values reported in [1]. A modest amount of NO_2 is also produced despite the lean conditions of this study, but these levels are significantly lower than those of NO and N_2O. In Figure 1 the mole fractions of NO and N_2O show some interesting behavior. From the images, it is clear that the dominant production of these species occurs in a neighborhood of the hotspots. However, with peak values of 1650 K and below, the temperatures are too low to support thermal NO formation. Once formed, NO appears to be quite stable, and the patterns of red shown in the figures indicate advection of the species far into the post-flame gas. The N_2O shows less uniform behavior across mixtures. In the leanest case, N_2O is produced consistently along the flame surface, and then remains in the gas without significant consumption downstream. For the richer mixtures, the N_2O concentration peaks uniformly near the wrinkled flame surface and then quickly decreases downstream in the hot gas.

Figure 2 shows vertical profiles of NO and N_2O over the bottom 10 cm of the domain, averaged over the horizontal coordinate and in time (using data for each that is taken after the flames have become statistically stationary). The plots include 1D steady flame profiles at the coresponding equivalence ratio. In each case, the concentrations of both NO and N_2O are higher in the post-flame region than in their 1D counterpart. At the flame surface, the sharp narrow peaks in NO of the 1D flame are broadened and reduced in the multidimensional cases due to the large spatial fluctuations in the position of the front. Although the total concentration of NO far downstream of the flame drops with decreasing equivalence ratio, amplification due to multidimensional effects increases. Mean values at the exit of the domain increase 33%, 66% and more than 200% for the $\phi = 0.45, 0.37$, and 0.30 cases, respectively. We believe that this nontrivial amplification of emissions across the range of mixtures represents a simple model for the unexpectedly large production of NO measured in lean H_2-air flames [20].

Figure 3 shows the consumption rate of H_2 and the production rates for NO and N_2O over the subregion near hotspots denoted by the white boxes in Figure 1. The images confirm that the dominant production of nitrogen oxides for all mixtures occurs in regions of intense burning and high temperatures.

Quantitative nitrogen path diagrams for each of the three cases, generated by integrating reaction rate data over the subregions depicted as white rectangles in Figure 3, are shown in Figure 4. Here, the arrow thicknesses are scaled linearly to the weight of the corresponding edge, normalized to the net transfer rate of nitrogen atoms from N_2 molecules in each case. As shown in the figure, the resulting graphs show a clear shift in the fate of reacting nitrogen atoms through these flames as a function of equivalence ratio. For the leanest case, $N_2 \rightarrow N_2O$ is the dominant N_2 destruction pathway, with $N_2 \rightarrow NNH$ playing a lesser but significant role. At $\phi = 0.37$ these roles are reversed. At $\phi = 0.45$, the destruction of N_2 is almost entirely through the $N_2 \rightarrow NNH$ path.

An interesting feature of Figure 3 is the multilayered structure of the NO production, which is most pronounced in the leaner $\phi = 0.30$ case. To help understand this behavior, Figure 5 shows the key contributions to the production of NO, as they vary along the white curves shown in Figure 3. The dotted black line in each case represents the sum of all contributions over the temperature range, while its integral over the entire range corresponds to the net sum of all edges into the node labelled "NO" in Figures 4(a) and (c).

Based on the results of Figure 5, as well as Figure 4, we can identify the mechanisms of NO formation in the present flames. The dominant mechanism, which becomes active when the temperature exceeds approximately 1000K, involves the NNH radical,

$$\mathrm{NNH} \rightleftharpoons \mathrm{N_2} + \mathrm{H} \qquad (\mathrm{R51})$$

$$\mathrm{NNH} + \mathrm{O} \rightleftharpoons \mathrm{NH} + \mathrm{NO} \qquad (\mathrm{R55})$$

$$\mathrm{NH} + \mathrm{O} \rightleftharpoons \mathrm{NO} + \mathrm{H} \qquad (\mathrm{R41})$$

and can be explained as follows. Over the entire temperature range, only R58b and R51b produce NNH. (The 'b' denotes that the reaction operates in reverse.) These are balanced almost completely by destruction via R57. The small remaining NNH production is balanced by a rather even distribution of R52-R56. Of these only R53 (producing N_2O) and R55 (producing NO and NH) move the nitrogen atoms into something other than N_2. Moreover, since R55 and R41 evolve in near lock-step, almost all of the nitrogen moving into NH through R55 continues to NO. Summing the three reactions formally, we obtain

$$\mathrm{R51b} + \mathrm{R41} + \mathrm{R55}: \quad \mathrm{N_2} + 2\mathrm{O} \rightleftharpoons 2\mathrm{NO}$$

confirming that the H and NH radicals are simply intermediates in the dominant route of NO production in the product stream. Note that in all cases, approximately 66% of the nitrogen from NNH that does not return directly to N_2 ends up in NO; the remainder ends up in N_2O. In the leaner case, N_2O is quite stable in the relatively cool exhaust gas, while for the richer case, much of the N_2O is converted back to N_2 before leaving the domain.

The $\phi = 0.30$ and $\phi = 0.45$ cases are interesting to compare here, because production of NO through the NNH route is considerably more effective in the richer case due to the elevated temperatures and enhanced atomic hydrogen concentrations, and this has a direct impact on the observed emissions. Another important observation is that NO production is actually significant throughout the temperature range, due to its involvement with the flame radicals, but this production is balanced locally by destruction over much of this region. At temperatures above 1100-1200 K, the NNH pathways become increasingly significant. Since there is no balancing destruction mechanism, most of the NO produced at high temperature advects uninhibited into the product stream.

In the cooler regions away from the hotspots, NO participates in a rapid interconversion with NO_2,

$$\mathrm{NO} + \mathrm{HO_2} \rightleftharpoons \mathrm{NO_2} + \mathrm{OH} \qquad \text{(R31)}$$

$$\mathrm{NO_2} + \mathrm{H} \rightleftharpoons \mathrm{NO} + \mathrm{OH} \qquad \text{(R32)}$$

These steps are the only significant reactions involving NO below approximately 1000 K. In this low-temperature region, the NO creation rate approximately balances the destruction, and the NO_2 concentration remains low. Formally, we can sum the two reactions obtaining

$$\mathrm{R31} + \mathrm{R32}: \quad \mathrm{H} + \mathrm{HO_2} \rightleftharpoons 2\mathrm{OH}$$

and deduce that where T <1000 K, NO and NO_2 simply play the role of intermediates in the conversion of H and HO_2 into two OH molecules. In essence R32 creates NO near 800K that is, for the most part, destroyed by reaction R31 near 600K. Moreover, whereas this chemistry is known to promote fuel oxidation [21], it is inconsequential under the present conditions, as it represents less than one part in 4000 of the total formation of OH in this region. In the hotter portion of the flame, NO created by R32 is locally balanced by destruction from R30 and R31.

The two most significant reactions producing N_2O are R35 and R53,

$$\mathrm{N_2} + \mathrm{O(+M)} \rightleftharpoons \mathrm{N_2O(+M)} \qquad \text{(R35b)}$$

$$\mathrm{NNH} + \mathrm{O} \rightleftharpoons \mathrm{N_2O} + \mathrm{H} \qquad \text{(R53)}$$

Again reflecting the path diagram analysis, for the leaner case, R35b, which produces N_2O from N_2, is more significant than the NNH pathway represented by R53. At the higher equivalence ratio the relative importance of these two reactions are reversed. In both cases, these production reactions compete with R37,

$$\mathrm{N_2O} + \mathrm{H} \rightleftharpoons \mathrm{N_2} + \mathrm{OH} \qquad \text{(R37)}$$

which converts N_2O back to molecular nitrogen. It is interesting to note that according to our calculations formation of NO through N_2O is of minor importance compared to the NNH mechanism. The reaction

$$\mathrm{N_2O} + \mathrm{H} \rightleftharpoons \mathrm{NH} + \mathrm{NO} \qquad \text{(R44b)}$$

proceeds in the reverse direction, forming N_2O rather than NO, and only the reaction

$$\mathrm{N_2O} + \mathrm{O} \rightleftharpoons \mathrm{NO} + \mathrm{NO} \qquad \text{(R38)}$$

serves to produce a little NO from N_2O.

The calculations show a shift in the ratio of NO to N_2O concentrations. For the leanest flames, the concentration of N_2O is a factor of five higher than that of NO at the exit plane. For $\phi = 0.37$ the concentrations of the two are roughly equal, while for the richest case the N_2O concentration is a factor of five smaller than that of NO. A key factor in this shift is the reduction in N_2O concentration behind the flame, apparent in Figure 1. While the data presented in figure 6 suggests that the key reactions for N_2O production shut down at high temperature, examination of the post-flame region shows that

$$\mathrm{N_2O(+M)} \rightleftharpoons \mathrm{N_2} + \mathrm{O(+M)} \qquad \text{(R35)}$$

reverses sign approximately 5 mm downstream of the intensely burning regions, converting the remaining N_2O back to N_2. The forward progress rate for R35 in these regions reaches values approximately 1/40$^{\mathrm{th}}$ of the peak negative value shown in figure 6, then decays very slowly in the product stream, decreasing by only a factor of 20 near the domain exit.

The indication of the present work that NNH rather than N_2O is the main precursor of NO in these lean premixed flames is a novel finding compared previous studies [5]. However, the balance between the NNH and N_2O mechanisms may shift towards N_2O as the pressure increases above atmospheric.

4. Conclusion

We have investigated the formation of nitrogen emissions in lean premixed hydrogen flames using two-dimensional numerical simulations of turbulent flame interactions. Although the simulations do not exhibit the plateau in emissions observed in experiments by Cheng *et al.* [1], they do show an increase in NO emissions relative to the laminar flame emissions that becomes increasing significant at lower equivalence ratios. At $\phi = 0.30$, the NO concentration is more than 3 times the value of the associated laminar flame. As expected, the increased production of emissions is associated with the enhanced combustion intensity resulting from the cellular structure of lean premixed hydrogen combustion. A detailed examination of the emission chemistry shows a shift in the dominant reaction pathways. At richer conditions, the predominant path for the initiation of emissions is $N_2 \rightarrow$ NNH. As the flame becomes leaner $N_2 \rightarrow N_2O$ becomes increasing important.

In future work we plan to extend this work to the higher turbulence intensities associated with the low swirl burner experiements. Three-dimensional simulations have shown that increased levels of turbulence lead to increased enhancement of the burning for lean hydrogen flames. Our goal will be to assess whether the more intense burning results in an increase in emissions that is sufficient to explain the plateau observed experimentally.

Acknowledgements

This work was suppored by the DOE Applied Mathematics Program under Contract No. DE-AC02-05CH11231.

References

[1] R. K. Cheng, D. Littlejohn, P. A. Strakey, T. Sidwell, *Proc. Combust. Inst.* 32 (2009) 3001–3009.

[2] D. Littlejohn, R. K. Cheng, *Proc. Combust. Inst.* 31 (2007) 3155–3162.

[3] M. Nakahara, T. Shirasuna, J. Hashimoto, *J. Thermal Sci. tech.* 4 (2009) 190–201.

[4] U. S. Dept. of Energy, Office of Fossil Energy, *Hydrogen from Coal Program: Research, Development and Demonstration Plan*, available at `http://fossil.energy.gov/programs/fuels/publications/programplans/2009_Draft_H2fromCoal_Sept30_web.pdf` (Sept. 2009).

[5] S. Correa, *Combust. Sci. Technol.* 87 (1992) 329–362.

[6] J. A. Miller, C. T. Bowman, *Prog. Energy Combust. Sci.* 15 (4) (1989) 287–338.

[7] E. Hawkes, J. H. Chen, *Combust. Flame* 138 (2004) 242–258.

[8] G. H. Markstein, *The Journal of Chemical Physics* 17 (4) (1949) 428–429.

[9] Y. B. Zeldovich, *Theory of Combustion and Detonation in Gases (in Russian)*, Acad. Sci. USSR, 1944.

[10] B. Bregeon, A. S. Gordon, F. A. Williams, *Combustion and Flame* 33 (1978) 33–45.

[11] T. Mitani, F. A. Williams, *Combust. Flame* 39 (1980) 169–190.

[12] M. S. Day, J. B. Bell, P.-T. Bremer, V. Pascucci, V. Beckner, M. Lijewski, *Combust. Flame* 156 (2009) 1035–1045.

[13] J. B. Bell, M. S. Day, J. F. Grcar, M. J. Lijewski, *Comm. App. Math. Comput. Sci.* 1 (1) (2005) 29–52.

[14] M. S. Day, J. B. Bell, *Combust. Theory Modelling* 4 (2000) 535–556.

[15] T. Mendiara, P. Glarborg, *Combustion and Flame* 156 (2009) 1937–1949.

[16] T. Mendiara, P. Glarborg, *Energ. Fuels* 23 (2009) 3565–3572.

[17] J. O. Hinze, *Turbulence*, 2nd Edition, McGraw-Hill, 1975.

[18] K. Yamamoto, M. Ozeki, N. Hayashi, H. Yamashita, *Proc. Comb. Inst.* 32 (2009) 1227–1235.

[19] Y. Rastigejev, M. Matalon, *J. Fluid. Mech.* 554 (2006) 371–392.

[20] R. K. Cheng, *Comb. Sci. Tech.*In press.

[21] P. Glarborg, *Proc. Combust. Inst.* 31 (2007) 77–98.

Table 1: Thermal and NNH/N_2O formation routes for NO.

No.	Reaction	A	n	E
30	$NO+O(+M) \rightleftharpoons NO_2(+M)$	1.3E15	-0.75	0
31	$NO+HO_2 \rightleftharpoons NO_2+OH$	2.1E12	0.00	-497
32	$NO_2+H \rightleftharpoons NO+OH$	1.3E14	0.00	362
33	$NO_2+O \rightleftharpoons NO+O_2$	1.1E14	-0.52	0
34	$2\ NO_2 \rightleftharpoons 2\ NO+O_2$	4.5E12	0.00	27599
35	$N_2O(+M) \rightleftharpoons N_2+O(+M)$	1.3E12	0.00	62570
36	$N_2O+H \rightleftharpoons N_2+OH$	3.3E10	0.00	4729
37	$N_2O+H \rightleftharpoons N_2+OH$	4.4E14	0.00	19254
38	$N_2O+O \rightleftharpoons NO+NO$	9.2E13	0.00	27679
39	$N_2O+O \rightleftharpoons N_2+O_2$	3.7E12	0.00	15936
40	$NH+H \rightleftharpoons N+H_2$	3.0E13	0.00	0
41	$NH+O \rightleftharpoons NO+H$	9.2E13	0.00	0
42	$NH+OH \rightleftharpoons N+H_2O$	5.0E11	0.50	2000
43	$NH+O_2 \rightleftharpoons NO+OH$	1.3E06	1.50	100
44	$NH+NO \rightleftharpoons N_2O+H$	2.9E14	-0.40	0
45	$NH+NO \rightleftharpoons N_2O+H$	-2.2E13	-0.23	0
46	$NH+NO \rightleftharpoons N_2+OH$	2.2E13	-0.23	0
47	$NH+NO_2 \rightleftharpoons N_2O+OH$	1.0E13	0.00	0
48	$N+OH \rightleftharpoons NO+H$	3.8E13	0.00	0
49	$N+O_2 \rightleftharpoons NO+O$	6.4E09	1.00	6280
50	$N+NO \rightleftharpoons N_2+O$	2.1E13	0.00	0
51	$NNH \rightleftharpoons N_2+H$	6.5E07	0.00	0
52	$NNH+H \rightleftharpoons N_2+H_2$	1.0E14	0.00	0
53	$NNH+O \rightleftharpoons N_2O+H$	1.0E14	0.00	0
54	$NNH+O \rightleftharpoons N_2+OH$	8.0E13	0.00	0
55	$NNH+O \rightleftharpoons NH+NO$	5.0E13	0.00	0
56	$NNH+OH \rightleftharpoons N_2+H_2O$	5.0E13	0.00	0
57	$NNH+O_2 \rightleftharpoons N_2+HO_2$	2.0E14	0.00	0
58	$NNH+O_2 \rightleftharpoons N_2+H+O_2$	5.0E13	0.00	0

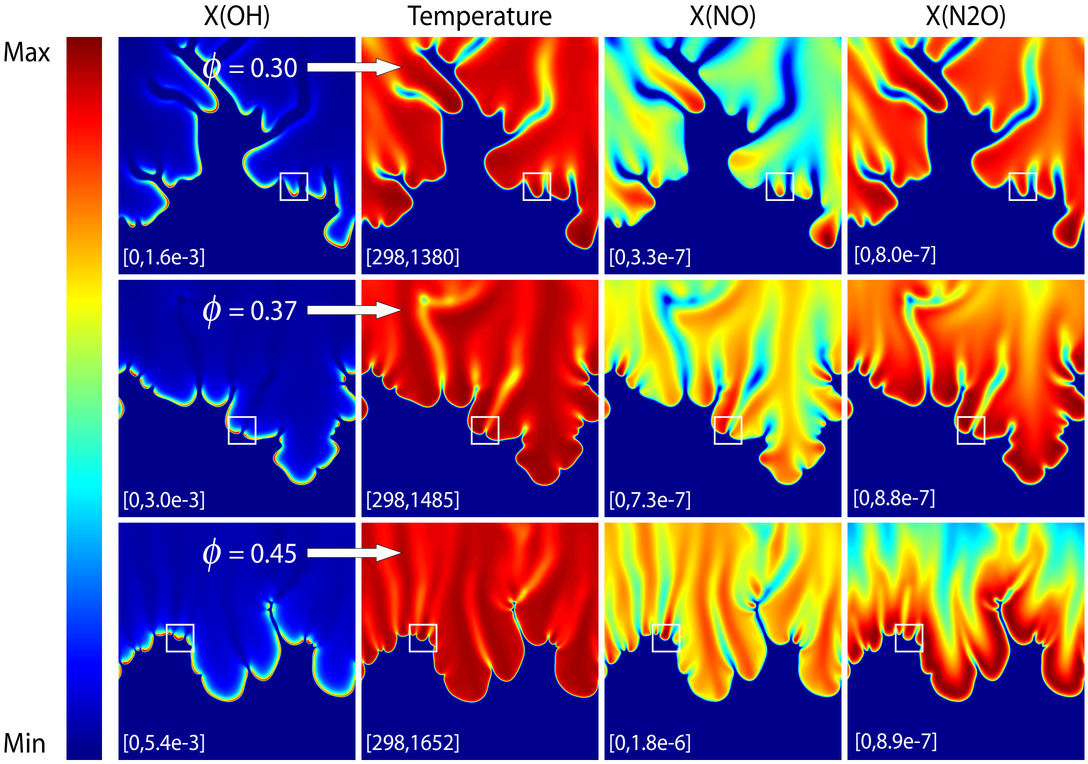

Fig. 1: Flame images showing X_{OH}, T, X_{NO} *and* X_{N2O} *over the bottom 8 cm × 8 cm of the computational domain for each of the three cases. The color bar range = [Min,Max] is specified on each image. The white inset boxes show the 9 mm × 9 mm subregion magnified for Figure 3 near a strongly burning cell.*

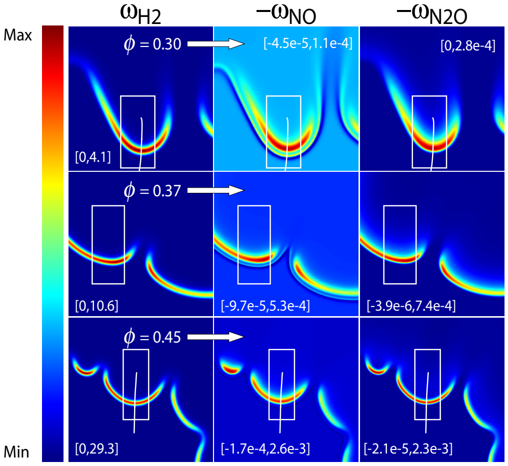

Fig. 3: Images of the production rate of H_2 and the destruction rates of NO and N_2O over the 9 mm boxes shown in Figure 1 near a strongly burning cell. The color bar range = [Min,Max] is specified on each image. The white boxes show the subvolume over an intensely burning region where data was extracted to construct the Nitrogen path diagrams shown in Figure 4. The white lines on the top and bottom and rows of figures show the location of the sampling normal used to construct Figures 5 and 6, respectively.

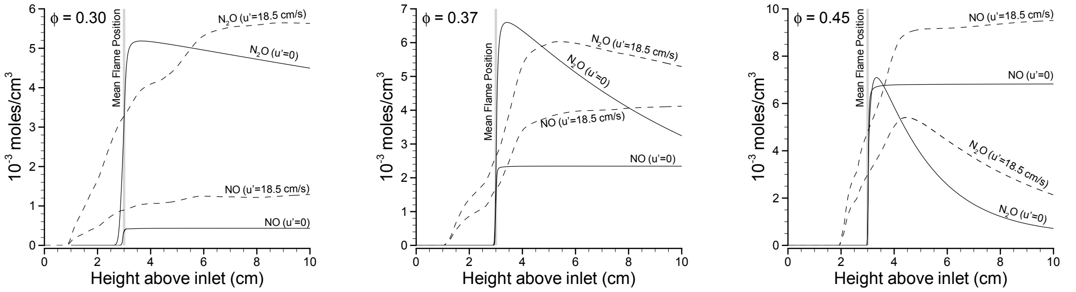

Fig. 2: Molar concentration of NO and NO$_2$, mean quasi-steady profiles from 2D simulations ($u' = 18.5$), amd from Premix ($u' = 0$).

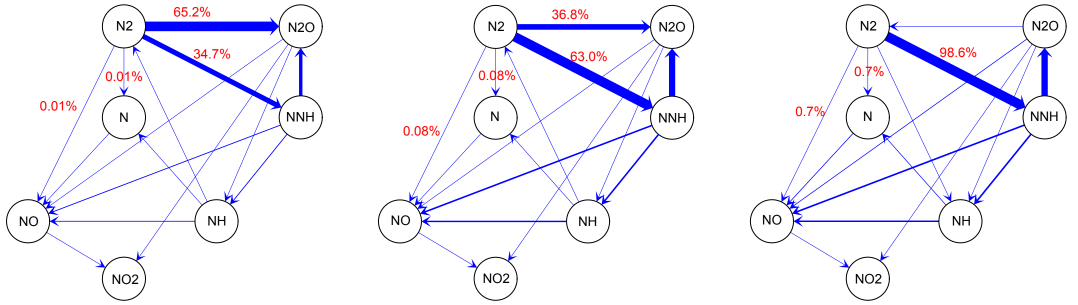

Fig. 4: Nitrogen atom pathway diagrams for boxed subregions shown in Figure 3. Arrows are proportional to the integrated transfer rate of N atoms between speices, and normalized to the total transfer rate of N atoms from N$_2$. Percentages indicate the fraction of N$_2$ destroyed along the various paths.

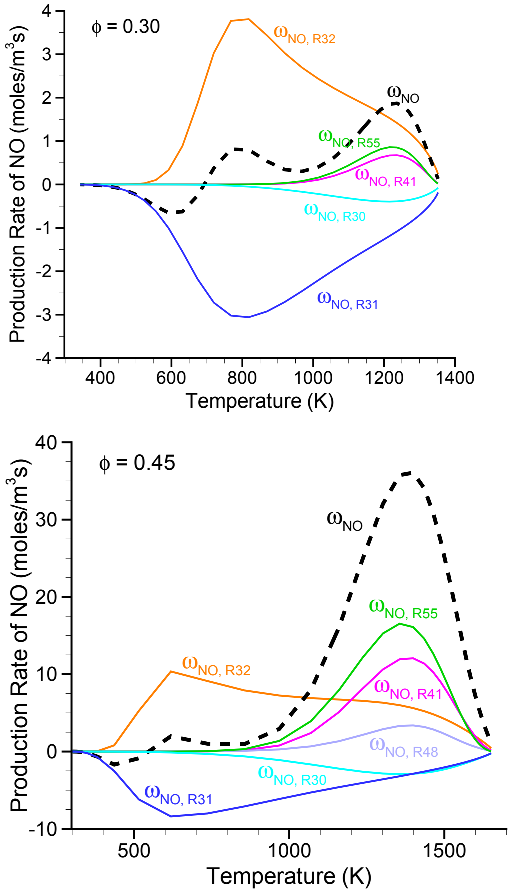

Fig. 5: Dominant contributions to the production of NO.

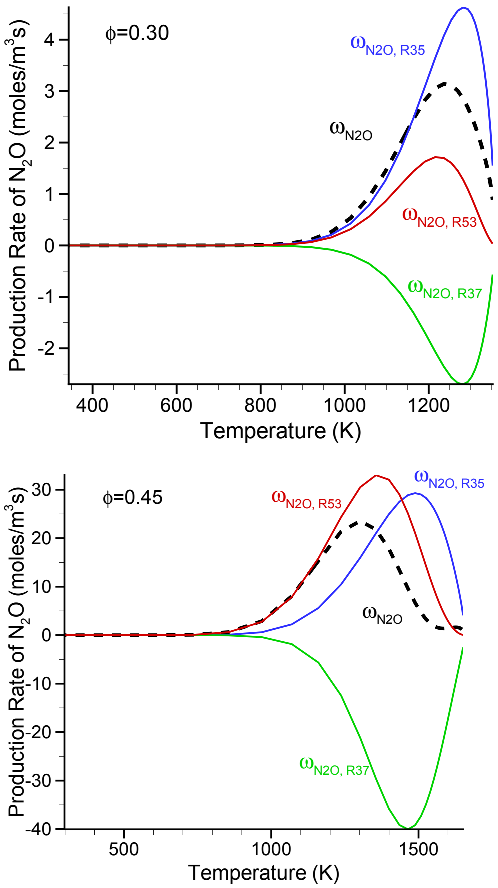

Fig. 6: Dominant contributions to the production of N_2O.